Structural Durability & Health Monitoring

Tech Science Press

https://doi.org/10.32604/sdhm.2026.079074

ARTICLE

Optimization Method for Sensor Placement in Fatigue Monitoring of Crane Welding Structures Based on Damage-Risk Fusion

Guansi Liu[1], Hui Jin[1,*], Keqin Ding[2], Hao Wang[3], Violeta Mircevska[4] and Maosen Cao[5]

[1]Jiangsu Key Laboratory of Engineering Mechanics, School of Civil Engineering, Southeast University, Nanjing, China
[2]China Special Equipment Inspection and Research Institute, Beijing, China
[3]Water Resources Research Institute of Shandong Province, Jinan, China
[4]University Ss. Cyril and Methodius, Skopje, North Macedonia
[5]Department of Engineering Mechanics, College of Mechanics and Engineering Science, Hohai University, Nanjing, China

*Corresponding Author: Hui Jin. Email: jinhui@seu.edu.cn

Received: 14 January 2026; Accepted: 12 March 2026; Published: 18 May 2026

ABSTRACT: In response to the dynamic changes in fatigue damage location of crane welding structures under lifting loads and the difficulty in accurately obtaining the stress concentration factor of welds, which results in limited effetiveness of traditional health monitoring sensor placement. This paper proposes aa sensor placement optimization method that integrates damage prediction and risk assessment. Firstly, the influence of weld geometry on fatigue performance is analyzed, and a rapid estimation model for the stress concentration factor is established using a radial basis function support vector machine. Furthermore, a fatigue damage prediction model for the welded structures is constructed. Secondly, the finite element simulation is employed to model typical crane operating conditions, and the structural stress distribution and cumulative fatigue damage are calculated. Considering the occurrence frequency of each operating condition in actual work, weighted cumulative damage is obtained. By identifying points with high weighted cumulative damage, quantifying their occurrence probability and consequences, and constructing a risk matrix, all potential fatigue points are ranked based on risk levels. Consequently, an optimal sensor placement method driven by both damage prediction and risk assessment is formed. Finally, the accuracy of the stress concentration factor estimation model is verified through a scaled model fatigue test of the main girder structure. The proposed sensor placement method for fatigue monitoring is further verified using a specific type of casting crane as a case study. The results indicate that the proposed method can effectively integrate damage information from multiple working conditions, characterize the structural damage status, and achieve optimized placement of sensors.

KEYWORDS: Crane; stress concentration factor; risk analysis; structural health monitoring; sensor arrangement

1 Introduction

Cranes are key equipment in the metallurgical industry. The operating conditions of metallurgical cranes are complex, and the time-varying nature of the lifting position and load leads to a dynamic spatiotemporal evolution of structural fatigue damage locations. As fatigue-sensitive areas, the stress distribution in weld zones is extremely uneven, and the degree of stress concentration is influenced by multiple factors such as weld size and joint type. The failure of a crane's steel structure often results in equipment damage, economic loss, and even personnel fatalities, which make its safe operation critically important [1]. Optimal sensor placement is a key aspect of structural health monitoring. Numerous scholars worldwide have conducted research on the theory and application of optimal sensor placement. Representative methods

include the Fisher information matrix method [2], the effective independence method [3], the genetic algorithm (GA) [4], the harmony search (HS) method [5], and the particle swarm optimization (PSO) algorithm [6]. Most of these methods aim to describe structural vibration modes with the fewest sensors, solving a mathematical problem for dynamic parameter identification [7,8], but they struggle to effectively capture the most likely fatigue failure locations of a structure under variable loads. Crane steel structures are primarily welded structures, and fatigue failure is one of the most predominant forms of failure in welded steel structures. In engineering practice, the stress concentration factor for welded joints is often determined by consulting manuals, which makes it difficult to reflect the local stress state of the actual weld, leading to significant calculation deviations. Numerical simulation based on finite element method can effectively analyze the influence of weld geometry details (such as weld leg length, weld toe angle, plate thickness, etc.) on stress distribution by constructing refined or parameterized finite element models. However, high fidelity 3D solid modeling and calculation are often time-consuming, labor-intensive, and costly. In recent years, artificial intelligence prediction models particularly those based on support vector machines, have shown great potential in the field of mechanical performance prediction [9–12]. Feng et al. [13] predicted the residual stress distribution of ship reinforced plate structures after induction heating, and the maximum relative error predicted by the SVM model based on radial basis functions was less than 5%. Gadallah and Shibahara [14] studied the effects of welding strength and load mode on the stress concentration factor of T-shaped butt welded joints of different base metal thin plates, revealing the influence of these parameters on the stress concentration factor. Melucci et al. [15] evaluated the changes in weld geometry using a dataset of laser scanning butt welds and obtained the correlation between weld geometry factors and fatigue life. Huang [16] studied the influence of factors such as stress concentration coefficient, surface coefficient, and size coefficient on the fatigue life of large structural components, and proposed a comprehensive fatigue correction factor for large structural components. However, the aforementioned studies primarily focus on material properties, static geometric parameters, or the analysis of effects under predetermined loads. The constructed models are still difficult to accurately capture the dynamic evolution of damage processes at the weld under actual variable load conditions, and they cannot achieve real-time mapping of stress concentration states under different manufacturing parameters and rapid assessment of cumulative damage considering load spectra. Moreover, the problem of how to optimally arrange sensors to capture these key damage signals under limited monitoring costs remains unsolved.

2 SVM-Based Stress Concentration Factor Estimation Model

2.1 Feature Parameter Selection and Dataset Construction

The stress concentration factor serves as a crucial bridge connecting between the nominal stress and the actual local stress at the weld seam. It is influenced by parameters such as the weld reinforcement angle, the base material thickness, and the radius at the weld toe. The transition from the weld seam to the base material in a T-joint is relatively abrupt, resulting in an extremely uneven distribution of working stress. Severe stress concentration exists at the weld toe of fillet welds. The geometric parameters of a typical T-joint are illustrated in Fig. 1.

The stress concentration factor at the weld toe of a T-joint can be expressed as [17]:

$$K_t = 1 + 0.35\left(\tan\theta\right)^{1/4}\left[1 + 1.1\left(c/l\right)^{3/5}\right]^{1/2}\left(\frac{t}{\rho}\right)^{1/2} \tag{1}$$

where, θ represents the toe angle, l represents the weld toe size, ρ represents the weld toe transition radius, c represents the main plate thickness, and t represents secondary plate thickness.

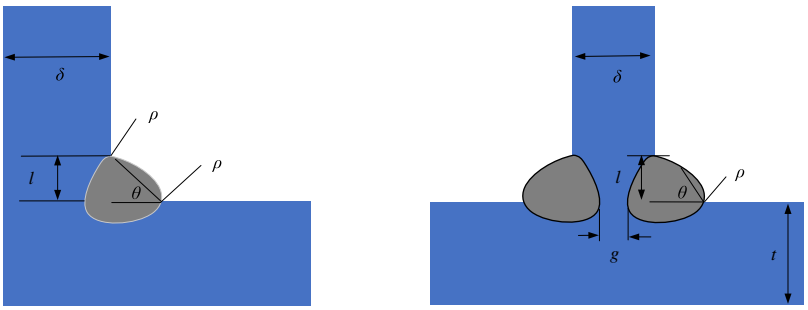

Figure 1: Schematic diagram of T-joint.

In the actual processing of crane box girder structures, an assembly gap h inevitably exists between the web and the lower cover plate, the web and the upper cover plate, and the web and the diaphragm, main girder, as shown in Fig. 2. An excessively large assembly gap can cause significant shrinkage deformation of the weld and also reduce the contact area between the weld material and the base material, assembly gap, thereby affecting the force distribution at the welded joint and impacting the fatigue life of the welded area.

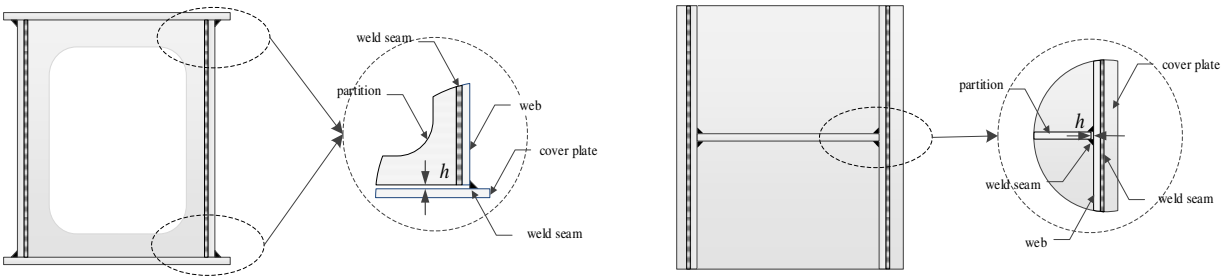

Figure 2: Schematic diagram of welding and assembly of crane box girder.

In order to investigate the influence of assembly gap h on stress concentration factors in various parts of the main girder structure, a solid model of the main girder and a weld model were established, with one end fixed and the other end releasing vertical degrees of freedom. The installation gaps in the model are set to 0, 0.2, 0.5, 1, 1.5, and 2 mm, respectively. The stress contours for the main girder and various weld seams are shown in Fig. 3.

Referring to Eq. (1), the nominal stress is taken as 133.73 MPa based on the experimental test value in reference [18]. The relationship curve between the stress concentration factor at the weld joint and assembly gap can be obtained comprehensively, as shown in Fig. 4.

Fig. 4 shows that there are optimal values for both assembly gap and weld toe angle, which can minimize stress concentration. As the size of the weld toe and the radius of the transition circle increase, stress concentration continues to decrease. There are significant differences in the stress concentration mechanisms of different types of welded joints (such as butt joints and load-bearing cross joints). Through analytical formulas, fine finite element analysis, or experiments, a corresponding dataset of geometric parameters (such as plate thickness difference, excess height, transition radius) of the target joint type (such as butt joints) and K_t can be collected. Using the same SVM algorithm, a specialized Kt prediction model for this joint type can be trained.

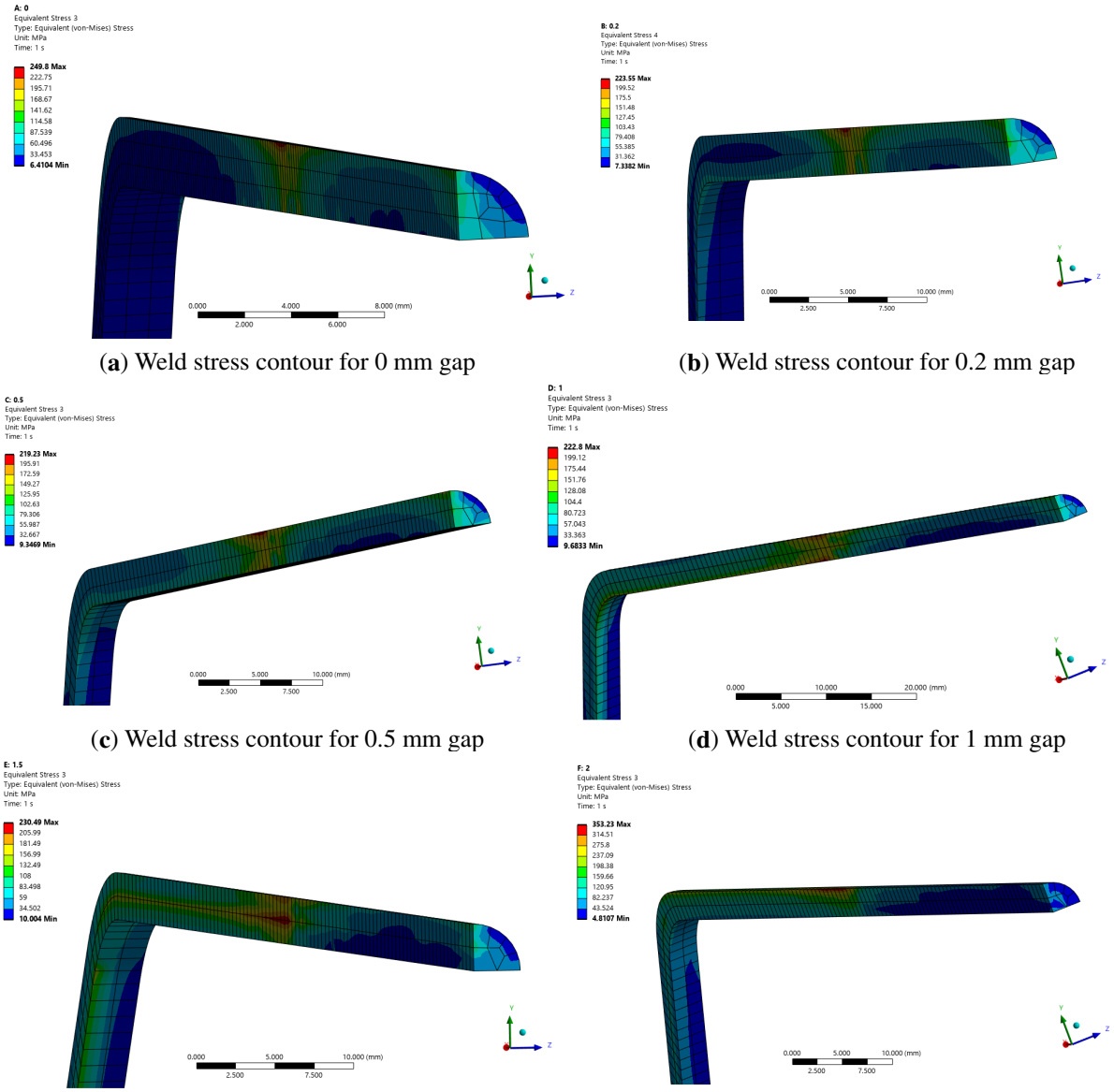

(**a**) Weld stress contour for 0 mm gap

(**b**) Weld stress contour for 0.2 mm gap

(**c**) Weld stress contour for 0.5 mm gap

(**d**) Weld stress contour for 1 mm gap

(**e**) Weld stress contour for 1.5 mm gap

(**f**) Weld stress contour for 2 mm gap

Figure 3: Weld stress contours for different assembly gaps.

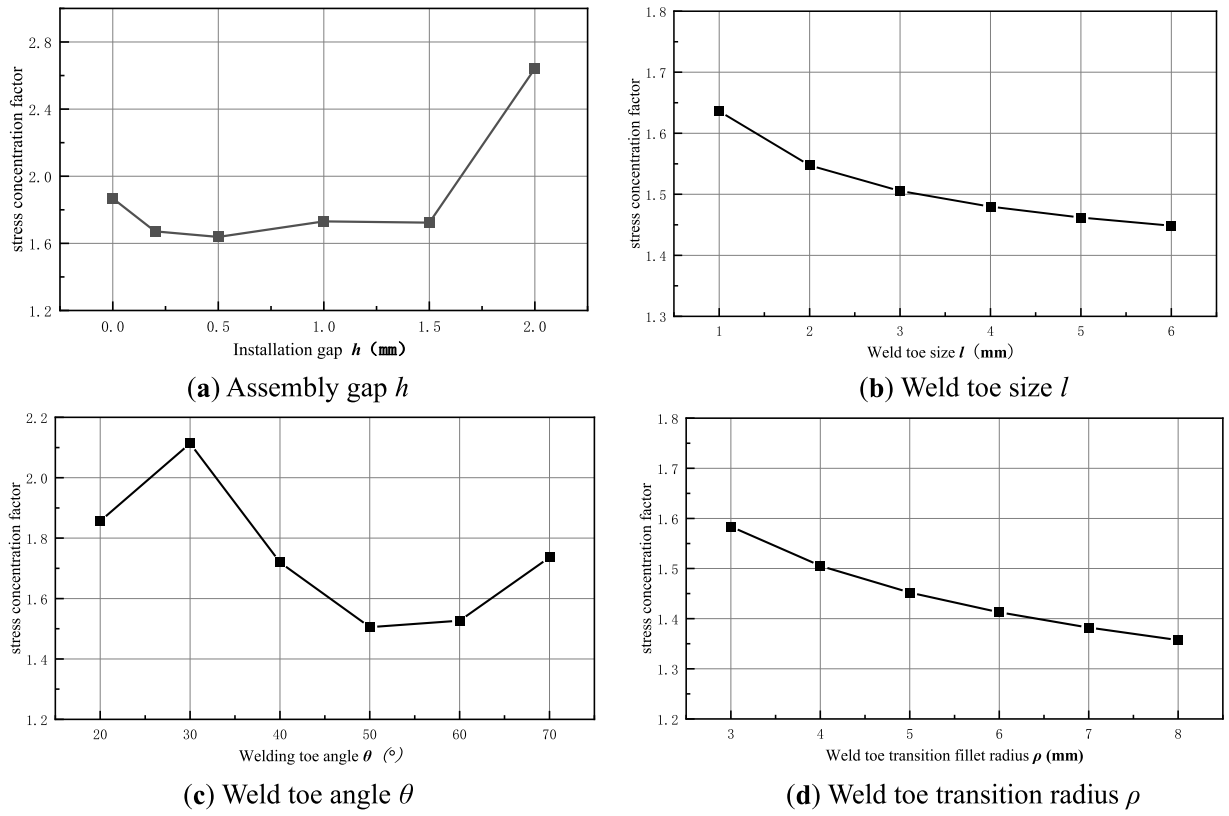

Figure 4: Relationship diagram between stress concentration factor and weld parameters.

2.2 SVM Model Training and Validation

To achieve real-time mapping of stress concentration states under different manufacturing parameters and rapid assessment of cumulative damage considering load spectra, a support vector machine (SVM) model can be used. SVM is a supervised learning method based on statistical learning theory, suitable for classification and regression analysis. It offers various kernel function options such as linear, polynomial, and radial basis functions, and can handle problems such as multi class classification, parameter optimization, and sample imbalance. SVM exhibits high computational efficiency, good prediction accuracy, and concise model structure when fitting the complex nonlinear relationship between stress concentration factor and multiple parameters such as assembly gap, weld toe size, weld toe angle, and transition radius. Once trained, the model can quickly and accurately output stress concentration factor estimates by inputting the geometric parameters of the weld seam, eliminating the need for repeated finite element simulations [19,20].

Given a training set $x_1, \ldots, x_n$, where represents sample features, $x = [h, l, \theta, \rho]$, y represents sample labels, stress concentration coefficient K_t, the goal of SVM is to find a hyperplane:

$$w^T x + b = 0 \tag{2}$$

where w is the normal vector of the hyperplane, and b is the bias term.

In order to make the model have good generalization ability, SVM seeks to maximize the minimum distance from the sample to the hyperplane, which can be represented by the following constraint conditions:

$$y_i \left(w^T x_i + b \right) \geq 1 \tag{3}$$

Under this constraint, SVM determines the optimal w and b by solving the following optimization problem:

$$\min_{w,b,\xi} \frac{1}{2} \|w\|^2 + C \sum_{i=1}^{n} \xi_i \tag{4}$$

In the equation, ξ_i is the relaxation variable.

In practical applications, data is often not linearly separable. To address this issue, SVM introduces a kernel function. By using a high-dimensional mapping, the raw data is mapped to a high-dimensional feature space, making the data linearly separable in the high-dimensional space. Using radial basis function (RBF Kernel) as the kernel function, its form is:

$$K\left(x_i, x_j\right) = e^{-\gamma \|x_i - x_j\|^2} \tag{5}$$

In the equation, γ is a parameter of the kernel function.

R^2 (coefficient of determination) represents the degree of fit of the model to the data. The calculation formula is:

$$R^2 = 1 - \frac{\sum_{i=1}^{n} \left(y_i - \overline{y}_i\right)^2}{\sum_{i=1}^{n} \left(y_i - \overline{y}\right)^2} \tag{6}$$

where $\overline{y}$ is the average of the true values. The closer R^2 is to 1, the stronger the explanatory power of the model on the data, that is, the better the model fits.

To establish a mapping relationship between assembly gap, weld toe size, weld toe angle, and weld toe transition radius and stress concentration factor, 221 sets of parameter stress concentration factor data obtained through analytical Eq. (1) and finite element calculation were used as the training set, and finite element calculation results were set as the test set. A prediction model based on Support Vector Machine (SVM) was constructed. The model uses radial basis functions as the kernel function and aims to minimize the root mean square error of the predicted values as the optimization objective. Systematic parameter optimization on the penalty factor C and kernel function parameter γ. The parameter search range is: C ∈ [0.1, 1, 10, 100], γ ∈ [0.01, 0.1, 1, 10]. The comparison of penalty factor and kernel function parameter grid search results is shown in Fig. 5, and the corresponding comparison of prediction accuracy and determination coefficient R^2 is presented in Fig. 6.

Fig. 5 shows that different penalty factors have a certain impact on the training set, but have little effect on the prediction results for the test set. From the coefficient of determination in Fig. 6, when the penalty factor is set to 10, there is a better linear correlation between the predicted values and the true values. If the penalty factor continues to increase, it will lead to excessively high model complexity, which can easily cause overfitting. The results indicate that the SVM model's prediction results are in good agreement with the theoretical values, and it can be effectively used for calculating the stress concentration factor of parameters such as assembly gap, weld toe size, weld toe angle, and weld toe transition radius.

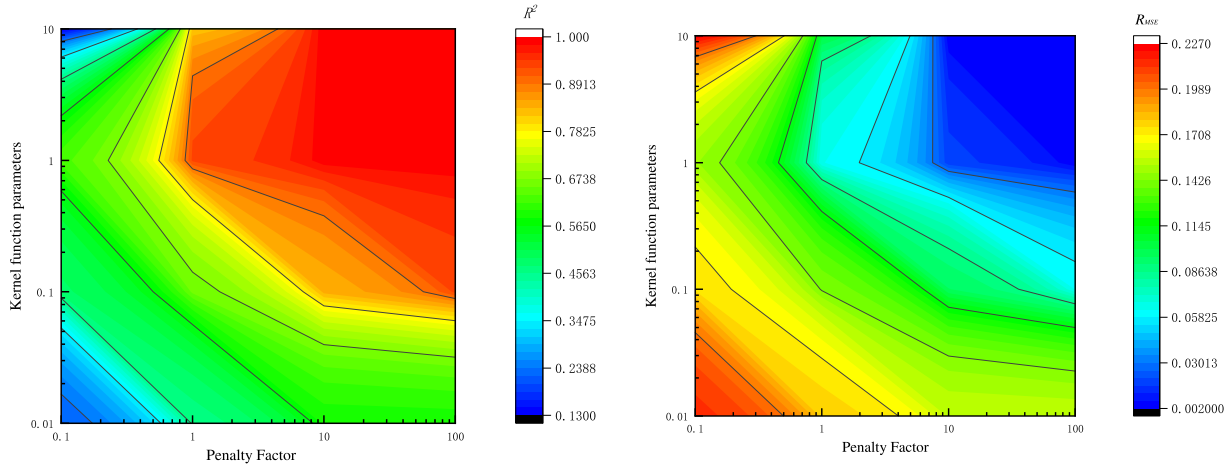

(**a**) Coefficient of determination (**b**) Root mean square error

Figure 5: Penalty factor and parameter grid search of kernel function.

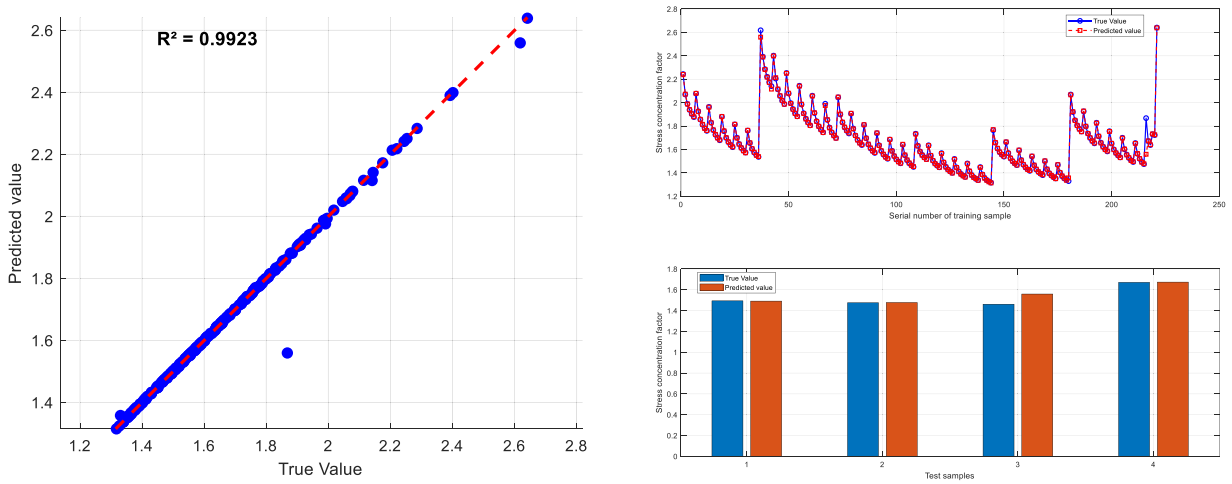

(**a**) Coefficient of determination (**b**) Prediction results

Figure 6: Punishment factor C = 10 and kernel function parameter γ = 0.8.

Therefore, Eq. (7) can be used to describe the relationship between the stress concentration factor and parameters such as assembly gap h, weld toe size l, weld toe angle θ, and weld toe transition radius ρ. The trained RBF-SVM model establishes a nonlinear mapping from the geometric parameter vector to the stress concentration factor:

$$K_t^{'} = SVM\left(h, \theta, \rho, l\right) \tag{7}$$

The trained RBF-SVM model provides an efficient tool for quickly calculating stress concentration factors for different weld details and conducting fatigue damage analysis under various working conditions. Different types of welded joints (such as butt joints, load-carrying cruciform joints) have significantly different stress concentration mechanisms. By collecting datasets correlating geometric parameters (e.g., plate thickness difference, reinforcement height, transition radius) with for the target joint type

(e.g., butt joint) through analytical formulas, detailed finite element analysis, or experiments, a dedicated prediction model for that joint type can be trained using the same SVM algorithm.

3 Risk Based Sensor Placement Optimization Method

3.1 Fatigue Damage Cumulative Calculation

After obtaining the stress concentration factor, the nominal stress method is used for damage calculation. The power function formula for fatigue analysis of steel structures is.

$$\left(S_{c0} \cdot K_{\sigma}\right)^{m} N = C \tag{8}$$

where C and m are material constants determined by experimental data; S_{c0} is the nominal stress acting on the part, and K_{σ} is the comprehensive correction factor.

Considering the working load factor, the following modified expression for fatigue strength can be obtained:

$$K_{\sigma}' = f\left(K_t', \beta, \varepsilon, C_L\right) = \frac{K_t'}{0.5\left[1 + \left(\frac{1}{88.3} \cdot \frac{L}{\overline{\overline{G}}}\right)^{-v_s}\right]} + \left(\frac{1}{\beta} - 1\right) \cdot \frac{1}{\varepsilon} \cdot C_L \tag{9}$$

where the constant v_s represents the sensitivity of the material to stress concentration and size, with smaller values indicating lower sensitivity to stress concentration. The range of v_s values for carbon steel is [0.1, 0.18]; The range of v_s values for alloy steel is [0.04, 0.12].

Substituting Eqs. (9) into (8) yields:

$$\left(S_{c0} \cdot K_{\sigma}'\right)^{m} N' = C \tag{10}$$

Taking logarithms on both sides of Eq. (10) and rearranging gives:

$$\lg N' = \lg C - m \cdot \lg\left(S_{c0} \cdot K_{\sigma}'\right) \tag{11}$$

Therefore, a new curve is obtained. Combined with the Miner's rule, the total damage D is the sum of damages from each stress amplitude level:

$$D = \sum_{i=1}^{n(t)} \frac{n_i}{N_i'} \tag{12}$$

where n_i represents the actual number of cycles at the i-th level stress amplitude, and N_i' represents the allowable number of cycles when fatigue failure is reached at the i-th level stress amplitude, obtained from the $S - N'$ curve.

3.2 Construction of Risk Matrix

To address the issues of inaccurate and excessive measurement points resulting from traditional static simulation-based sensor placement, the concept of risk is introduced to improve the monitoring logic from "static, empirical, local" to "dynamic, quantitative, global."

According to the probability of crane structural failure, it can be divided into five evaluation levels: Level 1 (unlikely to occur), Level 2 (very unlikely), Level 3 (moderate), Level 4 (high), and Level 5 (extremely likely). The cumulative damage degree D reflects the accumulation degree of fatigue damage under alternating loads

and is directly related to structural safety. When D = 1, the theoretical fatigue life of the structure is exhausted and cracks are generated [21]; When D = 0.5, the damage has reached half of the theoretical lifespan, and the risk of failure significantly increases; When D < 0.1, the risk of structural fatigue can be ignored.

Operation Frequency Statistics: By calculating the working cycle of the target crane (based on the stopping positions of the large and small vehicles), determine the relative frequency or probability p_i of the lifting load appearing at each typical position i, satisfying $\sum_{i=1}^{N} p_i = 1$. Accidental loads are random, high-amplitude, and low-cycle, making them difficult to incorporate into frequency analysis based on statistical typical conditions.

Damage weighted superposition: Multiply the damage value $D_{i,k}$ of the i-th position and k-th node by their corresponding job frequency p_i, and then superimpose the weighted damages of all N positions to obtain the weighted cumulative damage $D_{sum,k}$ of node k:

$$D_{sum,k} = \sum_{i=1}^{N} p_i * D_{i,k} \tag{13}$$

where $D_{i,k}$ represents the fatigue damage of the k-th unit in the i-th position of the structure, and p_i represents the frequency of the structure at the i-th position; $D_{sum,k}$ represents the weighted cumulative damage of the k-th node throughout the entire job cycle, which comprehensively reflects the load effect (magnitude) and load probability (frequency).

Probability level calculation: The calculated values $D_{sum,k}$ are sorted and used as the probability level for structural failure. In engineering, the cumulative damage level is usually classified based on industry safety standards and risk acceptance criteria. This study is based on a universal risk matrix framework, and divides the range of cumulative damage values into five progressive risk levels, as shown in Table 1.

Table 1: The correspondence between probability level and cumulative damage degree.

	Cumulative Damage Range	Engineering Meaning
Level 1	$D_{sum,k} < 0.1$	The damage is minimal and far from reaching the critical value; The fatigue risk can be ignored due to extremely low load or minimal frequency of use.
Level 2	$0.1 \leq D_{sum,k} < 0.3$	Low damage, the structure is in the early stage of safe life, and there is almost no possibility of failure under normal use.
Level 3	$0.3 \leq D_{sum,k} < 0.5$	Moderate damage, attention should be paid to load changes, entering the fatigue sensitive stage, and regular monitoring is required.

(Continued)

Table 1 (continued)

	Cumulative Damage Range	Engineering Meaning
Level 4	$0.5 \leq D_{sum,k} < 0.8$	The damage is significant, approaching the critical state, and the risk of failure increases. It is necessary to shorten the detection cycle and intervene.
Level 5	$D_{sum,k} \geq 0.8$	Severe damage, approaching or exceeding the fatigue life limit, may fail at any time, and must be immediately stopped for repair.

Referring to the Lifting appliances—Safety condition assessment risk estimation method. In the risk assessment of crane structures, the severity level of failure consequences is mainly divided based on its impact on structural integrity, functional safety, and the scope of accident impact. It can usually be divided into the following four levels, as shown in Table 2. The specific classification can also be adjusted according to the criticality of the actual equipment and user's risk acceptance criteria.

Table 2: Classification of safety consequences in typical areas of crane structures.

Consequence Level	Typical Area	Consequences of Failure
Level 1	Platform railing, non load bearing accessory welds	No local damage that directly affects safety
Level 2	Walking mechanism bracket, cab connection point	Function failure but can be temporarily repaired
Level 3	Main girder end welds, trolley frame load-bearing structure	Partial fracture leads to downtime and high maintenance costs
Level 4	Weld seams on the middle and lower cover plates of the main girder span, as well as the connection between the support legs and the main girder	Complete machine collapse, major safety accidents

After obtaining the probability level and consequence level of the risk factors affecting the metal structure of the crane, the final risk level needs to be determined through the risk matrix method, in order to qualitatively judge the degree of risk and provide decision-making basis for whether to install monitoring sensors. The calculation of risk value R is as follows:

$$R = P \times S \tag{14}$$

where P represents the probability level, with values [1, 5]; S represents the level of consequence, with values [1, 4].

According to Eq. (14), the range of risk levels can be obtained as [1, 20]. Further grading the risk level values and developing corresponding response measures for different grades. The risk matrix of crane

structure can refer to Table 3, or it can be classified according to the actual equipment usage scenario or user acceptance level.

Table 3: Crane structure risk matrix.

Risk Level		Probability Level				
		1	**2**	**3**	**4**	**5**
Consequence level	1	1	2	3	4	5
	2	2	4	6	8	10
	3	3	6	9	12	15
	4	4	8	12	16	20

The different colors in Table 3 represent different risk levels, green indicating low risk and yellow indicating moderate risk, orange indicates high risk, and red indicates extremely high risk. The calculation of risk value is shown in Eq. (14), where P represents the probability level, with values [1, 5]; S represents the level of consequence, with values [1, 4].

Green indicates low risk and does not require the deployment of monitoring sensors. Routine inspections should be conducted according to standard management procedures; Yellow is considered medium risk and does not require the installation of monitoring sensors, but it is necessary to regularly monitor the dynamic changes in accumulated damage; Orange indicates high risk, requiring the deployment of monitoring sensors and regular monitoring of accumulated damage changes; Red indicates extremely high risk, and monitoring sensors must be installed. To reduce subjective influence, it is recommended to adopt a conservative principle of "high rather than low" for areas with fuzzy boundaries in practical applications, to ensure that high-risk points are not overlooked.

3.3 Risk Based Sensor Placement Optimization Strategy

The final arrangement of sensors is the process of optimizing resource allocation, with the goal of obtaining maximum structural health information with the least number of sensors. Propose the following hierarchical placement strategy:

(1) Determine the analyzed structure, clarify the position and type of weld seam;
(2) Combine design and process parameters to determine weld-related parameters such as assembly gap, weld toe angle, weld toe size, and transition radius. Call the trained RBF-SVM model (Eq. (7)) to calculate the stress concentration factor for each weld.
(3) Combine process parameters and usage conditions, determine the structural component size factor, structural surface quality factor, loading conditions, welding residual stress, and other factors for each weld seam of the analyzed structure. Calculate the comprehensive correction factor K'_σ for each region according to Eq. (9);
(4) Construct a finite element model of the analyzed structure and conduct fatigue analysis under typical working conditions. Redefine the S-N curve of the structure according to Eq. (11), calculate the number of cycles for each region under different stress amplitudes according to Eq. (12), and further determine the cumulative damage D at each point using the Miner cumulative damage criterion;
(5) Calculate the weighted cumulative damage of each node throughout the entire job cycle according to Eq. (13), sort them according to the size of the weighted cumulative damage, and determine their positions;

(6) Determine the probability level P and consequence level S based on $D_{sum,k}$ (Table 2), and combine it with the crane structure risk matrix (Table 3) to determine the risk level of the structure. Rank all parts according to risk and clarify the monitoring points for extremely high risk and high risk. The allocation principle of the number of sensors in the area: For a large high-risk area, if the risk analysis or finite element cloud map shows a clear damage gradient inside, no less than 2 sensors should be arranged in the area to capture the most dangerous points and damage distribution characteristics. If there are multiple potential failure modes and different stress paths in the area, multiple sensors should be considered to distinguish the damage of different modes.

(7) Based on the real-time collection of strain time history data from the monitoring points mentioned above, the stress cycle is calculated using the rainflow counting method, and the damage increment ΔD is calculated using the K_t determined in step (2) and the corrected S-N curve determined in step (4). The probability level P is updated in real-time based on the total cumulative damage.

(8) Regularly update the probability level P and the consequence level S (Table 2), and recalculate the risk value R (Eq. (14)). When the risk level of a certain measuring point transitions or the cumulative damage rate exceeds the preset threshold, the system automatically triggers a graded warning to provide decision support for preventive maintenance. For the "medium risk" areas without installed sensors, estimate the time required for the damage to develop from the current value to the warning threshold based on their weighted cumulative damage value D and assumed average damage growth rate, determine the inspection interval, and revise the damage growth model based on the damage data of adjacent monitored areas during each inspection. If the inspection shows no abnormality and the damage growth prediction is stable, the inspection interval can be appropriately extended; otherwise, it should be shortened.

4 Experimental Verification and Engineering Application Analysis

4.1 Verification of Scaled Model Fatigue Test

To verify the accuracy of the fatigue damage prediction model proposed in this article, a scaled model of typical welded joints of crane box girder was designed and fabricated. The model adopts Q345 with a similarity ratio of 1:12. The scaled main girder had a length of 2000 mm, a width of 220 mm, and a height of 230 mm, with a plate thickness of 6 mm. Ten diaphragms were uniformly arranged along the axial direction of the main girder. The three-dimensional model of the main girder structure is shown in Fig. 7. The physical model is shown in Fig. 8.

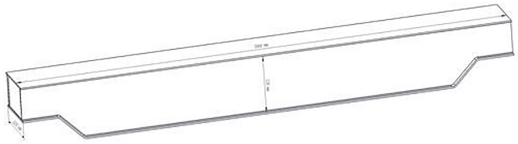

Figure 7: 3D model diagram of main girder structure.

Figure 8: Physical picture of the main girder model.

The main girder is welded to the upper and lower cover plates through a single-sided corner weld, with a weld installation gap of 1.5 mm, a weld toe angle of 45°, a transition radius of 3 mm, and a weld toe size of 3 mm. By substituting Eq. (7).

$$K_t^{'} = SVM\left(h, \theta, \rho, l\right) = SVM\left(1.5, 45, 3, 3\right) = 1.73 \tag{15}$$

The surface of the crane steel structure is treated with anti-corrosion paint, and the surface state coefficient is taken as β with a value of 0.87. The structural thickness t is 6 mm and the cross-sectional size that can withstand tensile and compressive loads is relatively large, so the size effect needs to be considered. According to the table, the size coefficient ε is taken as 0.85; The main girder structure mainly bears tensile and compressive loads, with a load coefficient C_L of 1 for both tension and compression; According to the basic dimensions of the notched specimen, the value of $L/\overline{G}$ is 12, and for carbon steel v_s is 0.1. Combining Eq. (9), the revised comprehensive influencing factor can be obtained as follows:

$$\begin{aligned} K_\sigma' = f\left(K_t, \beta, \varepsilon, C_L\right) &= \frac{K_t^{'}}{0.5 \cdot \left[1 + \left(\frac{1}{88.3} \cdot \frac{L}{\overline{G}}\right)^{-v_s}\right]} + \left(\frac{1}{\beta} - 1\right) \cdot \frac{1}{\varepsilon} \cdot C_L \\ &= \frac{1.73}{0.5 \cdot \left[1 + \left(\frac{1}{88.3} \cdot 12\right)^{-0.1}\right]} + \left(\frac{1}{0.87} - 1\right) \cdot \frac{1}{0.85} \cdot 1 = 1.73 \end{aligned} \tag{16}$$

The expression of the modified structure S-N in the double logarithmic coordinate system is:

$$\lg N' = 10.8165 - 3 \times \lg(1.73 \times \sigma) = 10.1024 - 3 \times \lg \sigma \tag{17}$$

The fatigue cumulative damage of the main girder before and after correction was calculated using finite element method, as shown in Fig. 9.

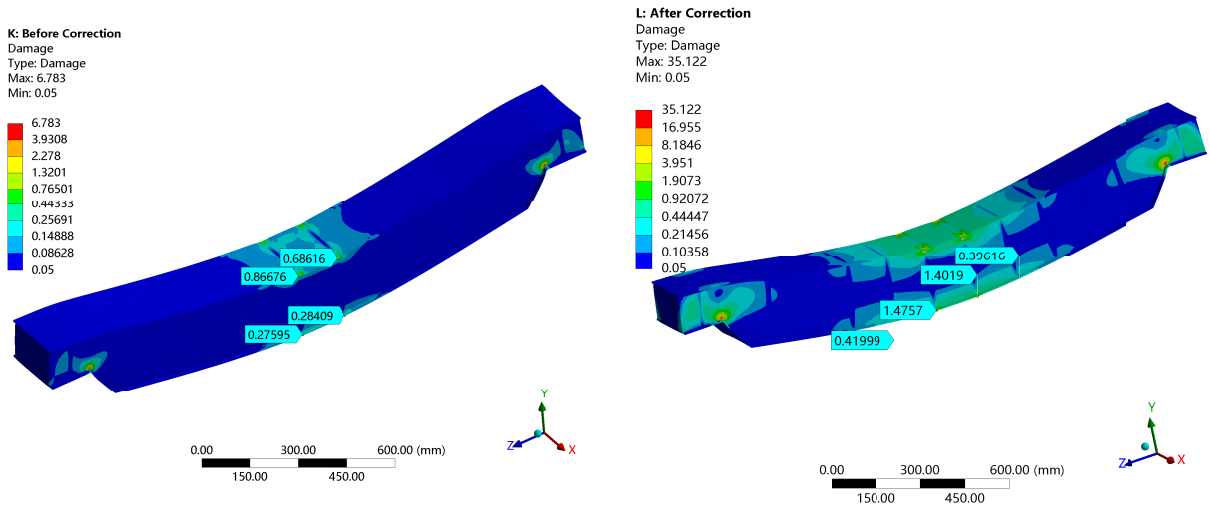

(**a**) Damage cloud map before correction (**b**) Revised damage cloud map

Figure 9: Comparison of damage cloud maps before and after correcting the S-N curve.

Fatigue tests were performed on the specimen using an Instron electro-hydraulic servo fatigue testing machine and a digital signal processor. Both ends of the main girder were supported on matching supports,

with one end fixed and the other end constrained in vertical and lateral displacements. The field test is shown in Fig. 10.

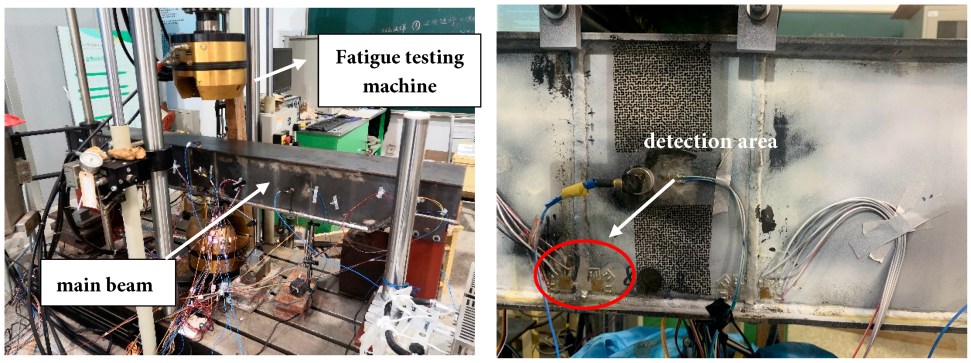

Figure 10: Experimental loading test diagram.

The maximum positive bending moment borne by the mid span of the main girder is one of the weakest and most stressed areas of the main girder. Therefore, during the fatigue test, the mid span area of the main girder is selected as the detection area. As the position of the upper cover plate is close to the load in use position, the following cover plate positions are used as the detection area for analysis. The test detection area is shown in Fig. 10. Perform non-destructive testing on the 50,000th and 100,000th shutdown cycles of the test, and the results of the non-destructive testing are shown in Fig. 11.

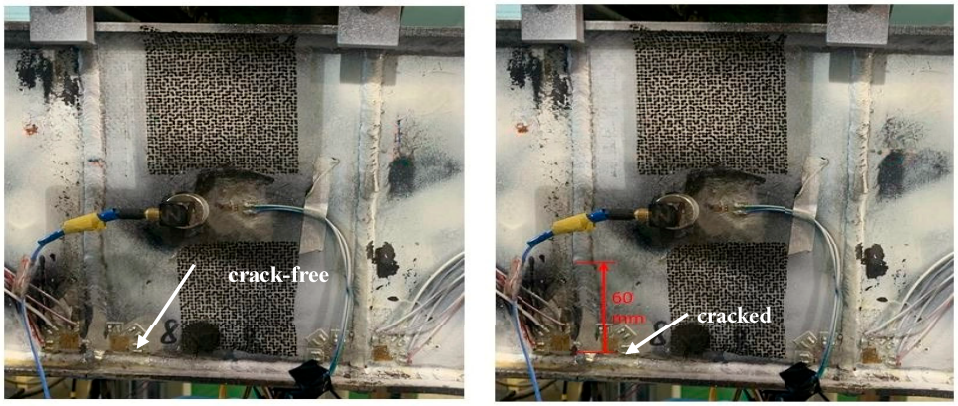

(**a**) Cycle loading 50,000 times (**b**) Cycle loading 100,000 times

Figure 11: Non destructive testing results after cyclic loading.

Fig. 11 shows that after 50,000 loading cycles, no cracks were found in the weld connecting the web and the diaphragm at mid-span. After 100,000 loading cycles, cracks appeared in the weld connecting the web and the diaphragm at mid-span of the main girder structure, and the cracks propagated upwards along the weld to 60 mm. The fatigue cycle numbers calculated for the inspection area at the mid-span of the scaled model main girder using different modeling methods are shown in Table 4 main girder.

The equivalent stress of the structure is 56.66 MPa. The traditional model has undergone over 360,000 cycles under this stress amplitude, while the modified model has undergone approximately 70,000 cycles. The experimental model developed cracks after 50,000 cycles, and the modified model is more consistent with the experimental model. Therefore, the modified model can be used to predict the fatigue life of crane structures.

Table 4: Comparison of results from different fatigue life methods.

Model Approach	Traditional Model	Revise the Model	Test Model
Number of cycles	360,305	69,594	50,000~100,000

4.2 Application of Optimized Sensor Placement for a Certain Casting Crane

A casting crane manufactured in 2003 at a steel plant was used as the test object for monitoring. The equipment has a span of 23.5 m and a working class of A7. It has been in use since July 2004. The web of the main girder is welded to the upper and lower cover plates through a single-sided corner weld, with a weld assembly gap of 2 mm, a weld toe angle of 45°, a transition radius of 2 mm, and a weld toe size of 8 mm. By substituting the stress concentration factor into Eq. (7), the stress concentration factor at the weld site can be obtained as 1.734. Furthermore, by substituting the stress concentration factor into Eq. (9), the revised comprehensive influence factor can be obtained as 1.734. Metallurgical cranes serve continuous smelting production. Their operating objects (ladle weight) and operation cycles are relatively fixed, exhibiting short-term stability of the operating conditions. Based on historical homework logs, the relative frequencies of the left, middle, and right typical positions are determined to be 1:2:1, with probabilities of [0.25, 0.5, 0.25] for the left, middle, and right positions. A finite element model is constructed to calculate the fatigue cumulative damage at the typical positions, and the weighted cumulative damage under typical operating conditions is obtained according to Eq. (13). Then, based on typical operating conditions, calculate the cumulative fatigue damage at each location as shown in Fig. 12 main girder transition radius.

The probability level P and consequence level S (Table 2) are determined based on $D_{sum,k}$. Combining these with the crane structure risk matrix (Table 3), the risk level of the structure is judged. Risk ranking is performed for all locations, identifying extremely high-risk and high-risk monitoring points. The crane bridge structure can be divided into three parts, namely the main girder, the auxiliary main girder, and the end beam. From Fig. 12, it can be seen that the area with the greatest damage is located at the connection between the main girder and the end beam, followed by the main girder. Further combining with the risk matrix constructed in Section 3.2, the risk classification of different areas of the crane bridge structure can be obtained as shown in Table 5.

Based on the maximum damage criterion method, sensors are arranged in the maximum damage area of three working conditions. Fig. 12a–c determine the monitoring area as the connection between the main girder and the end girder; Through the weighted superposition of multi condition damage as shown in Fig. 12d damage cloud map, it can be seen that the monitoring area includes the connection between the main girder and the end girder (extremely high risk), the mid span area of the main girder (extremely high risk), and the quarter span area of the main girder (high risk). The analysis shows that the traditional method is only based on the damage cloud map of a single most dangerous working condition, and all the sensors are concentrated in the part of "the connection between the main girder and the end girder". The risk-based optimal placement method uses the multi-case weighting and risk matrix, which can be used to determine the optimal locations of the sensors, several key risk areas were identified, such as "Mid-span of main girder" (extremely high risk), "Quarter-span of main girder" (high risk), and "Connection between main girder and end girder". The risk-based method identified three key risk areas (mid-span-very high risk, end connection of main girder-very high risk, and 1/4 span-high risk), the maximum damage criterion identifies only one area (the end connection of the main girder), and the coverage of the risk-based method is twice that of the traditional method in the case of the same two points.

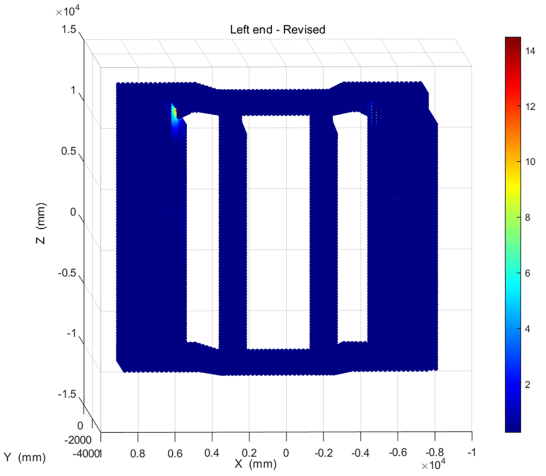

(**a**) Left end working condition damage cloud map

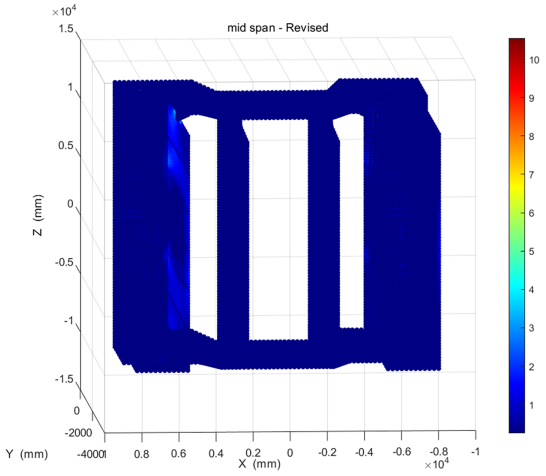

(**b**) Cloud map of damage in mid span working conditions

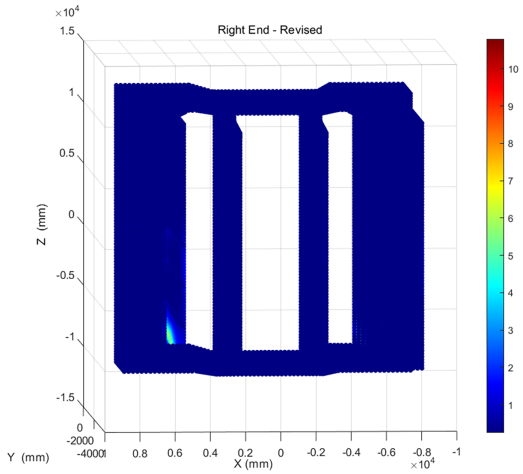

(**c**) Right end working condition damage cloud map

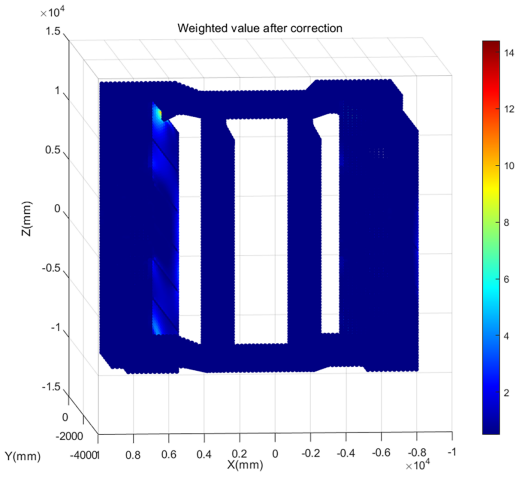

(**d**) Weighted damage cloud map of bridge frame

Figure 12: Revised fatigue cumulative damage cloud map of bridge frame.

Table 5: Risk analysis of crane bridge structure in different areas.

Bridge Structure	Probability Level	Consequence Level	Risk Level	Matrix Color Chart
Main girder mid span	5	4	20	Red
Quarter span of main girder	3	4	12	Orange
Middle span area of secondary main girder	2	3	6	Yellow
Sub main girder quarter span area	2	3	6	Yellow
End beam	2	3	6	Yellow
Main girder and end beam connection part	5	4	20	Red

(Continued)

Table 5 (continued)

Bridge Structure	Probability Level	Consequence Level	Risk Level	Matrix Color Chart
Secondary main girder and end beam connection part	2	3	6	Yellow

Metallurgical plants contain strong electromagnetic interference sources such as high-current motors and variable frequency devices. Traditional resistance strain gauges are susceptible to this interference, while Fiber Bragg Grating (FBG) sensors are inherently immune to electromagnetic interference, ensuring a good signal-to-noise ratio. Therefore, fiber Bragg grating strain sensors were used for monitoring, and temperature sensors were arranged to compensate for temperature effects. The sensors were connected via armored optical cables, and the monitoring host was placed inside the main girder chamber. The connection area between the main girder and the auxiliary main girder had been previously modified. Sensors were arranged in the main girder mid-span area, the main girder quarter-span area, and the main girder end connection. Obtain the stress history curve of the main beam and the stress time history curves of each monitoring sensor, with one day's curve shown in Fig. 13.

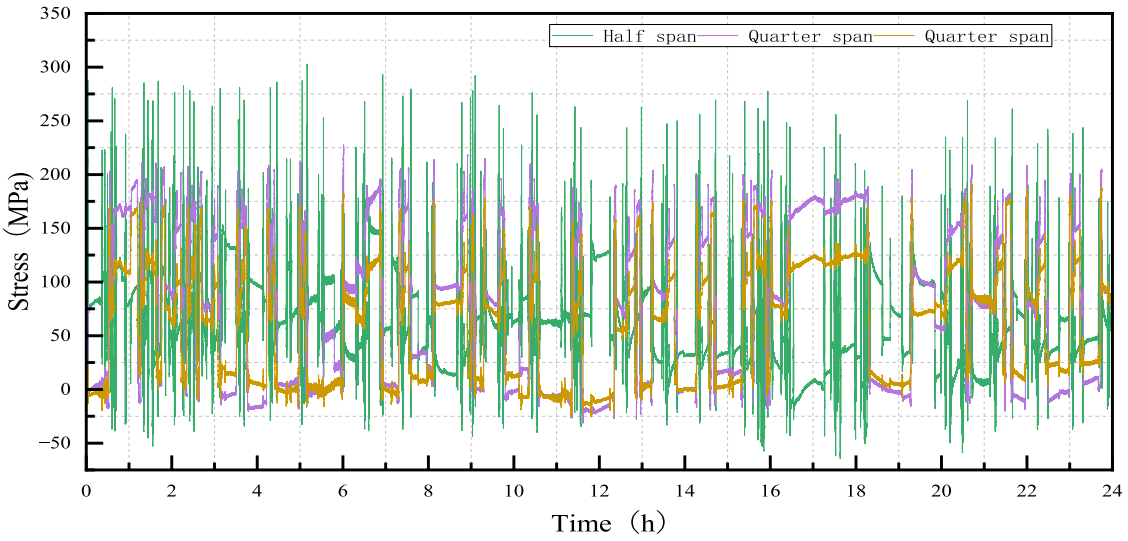

Figure 13: Stress time history curve of each measuring point.

The average annual operating time of metallurgical cranes is about 180 days, and their operating objects (ladle weight) and operating cycles are relatively fixed, with stability in short-term working conditions. The rainflow counting method was used to statistically process the stress time history data collected from each measuring point. According to GB/T33218-2016 and combined with Eq. (11) for fatigue analysis, the cumulative fatigue damage of each measuring point is shown in Table 6.

Table 6: Damage and lifespan of each measuring point.

Sensor Position	Accumulated Damage (days)	Fatigue Life (Years)	Remaining Useful Life (Years)
Half span	2.84×10^{-4}	25.5	4.5
Quarter span	1.04×10^{-5}	>>30	>>30
Quarter span	2.81×10^{-6}	>>30	>>30

Through monitoring data calculations, it can be found that half of the span has the greatest damage, and the estimated remaining life of the structure under this condition is 4.5 years. This is consistent with the conclusion emphasized by the risk-based placement strategy that the mid span of the main girder is a high-risk area. The reason is that half of the span is subjected to high amplitude bending normal stress cycles, and the damage is mainly dominated by low-frequency large amplitude fluctuations, at the connection between the web plate and the lower cover plate (maximum tensile stress zone); The composite stress cycles of quarter span and quarter span, combined with high-frequency impact and medium amplitude fluctuations, result in relatively fast accumulation of fatigue damage. The difference between the two measuring points is that the quarter span (left) experiences more full load conditions, resulting in greater cumulative damage and shorter remaining life.

5 Conclusion

Addressing the challenge of monitoring fatigue damage in crane welded structures under dynamic loads, this paper integrates risk assessment and cumulative damage analysis to form an engineering application method for optimal sensor placement. Its feasibility was verified through experiments and an engineering case study. The main conclusions are as follows:

(1) A rapid estimation model for weld stress concentration factors based on RBF-SVM was constructed. This model can quickly predict the stress concentration factor based on weld geometric parameters (assembly gap, weld toe size, weld toe angle, transition radius), with prediction accuracy meeting engineering requirements (coefficient of determination $R^2 > 95\%$). Compared to traditional manual lookup or detailed finite element analysis, this method offers advantages in computational efficiency and adaptability, supporting subsequent damage calculations under multiple operating conditions. Scaled model tests preliminarily verified the model's applicability. However, the size effects of welding residual stress and micro-defects are difficult to fully replicate in scaled models; engineering applications still require calibration with non-destructive testing results from full-scale structures.

(2) An assessment framework integrating multi-condition weighted cumulative damage and risk quantification was established. By introducing operation frequencies to weight and superpose damage under typical operating conditions, a cumulative damage distribution reflecting the actual service history was obtained. This cumulative damage was then quantified into a failure probability level and combined with a consequence level based on structural importance. Using a risk matrix, risk ranking of various structural parts was achieved, transforming the monitoring objective from "capturing the maximum damage point" to "covering the highest risk areas."

(3) A decision-making criterion for sensor placement based on risk classification was proposed. Based on risk levels and damage evolution characteristics, a layered placement strategy was formed: "prioritize monitoring for extremely high-risk areas, selectively monitor high-risk areas, and conduct regular inspections for medium and low-risk areas". Application on a specific casting crane showed that this

strategy effectively identified key risk areas such as the main girder mid-span, quarter-span, and end connections. Compared to a placement method based solely on a single maximum damage point, it achieved broader coverage of critical areas with limited sensor resources.

Acknowledgement: The authors would like to thank all individuals and organizations that contributed to this study through administrative and technical assistance, as well as material or equipment support. Their contributions were essential to the successful completion of this research.

Funding Statement: This research was supported by National key technologies Research & Development program through 2024YFC3014900.

Author Contributions: Guansi Liu is responsible for writing the first draft of the paper, the code implementation of the core algorithm and the preliminary simulation verification. Keqin Ding is in charge of the overall structure design and writing plan of the thesis. Hui Jin is responsible for guiding the algorithm implementation strategy, optimizing the simulation scheme, and reviewing and revising the paper. Hao Wang is responsible for guiding the experiment and data collection. Violeta Mircevska is responsible for building the architecture of the paper, while Maosen Cao is responsible for designing and guiding the overall idea of the paper. All authors reviewed and approved the final version of the manuscript.

Availability of Data and Materials: The data used to support the findings of the study are available from the corresponding author upon request.

Ethics Approval: Not applicable.

Conflicts of Interest: The authors declare no conflicts of interest.

References

1. Guo Y, Rao G, Dang Z, Zhang R, Luo H, Yuan R. Fracture mechanism analysis and life-prolonging investigation of butt weld for ladle crane. Eng Fail Anal. 2025;172:109389. doi:10.1016/j.Engfailanal.2025.109389.
2. Geonho S, Jangwook H. Correlation coefficient based optimal vibration sensor placement and number. J Sens. 2022;22(3):1207. doi:10.3390/s22031207.
3. Lee ET, Eun HC. An optimal sensor layout using the frequency response function data within a wide range of frequencies. Sensors. 2022;22(10):3778. doi:10.3390/s22103778.
4. Zhang ZY, Li XH, Dan DH. Optimal sensor placement for bridge using the improved genetic algorithm. Constr Technol. 2025;54(21):64–71. doi:10.7672/sgjs2025210064.
5. Liu G, Ding K, Jin H, Tang F, Chen L. Sensor layout of hoisting machinery vibration monitoring based on harmony genetic search algorithm. Struct Durab Health Monit. 2022;16(2):145–61. doi:10.32604/sdhm.2022.022241.
6. Zhen Z. Optimal layout of health monitoring sensor in gymnasium based on improved particle swarm optimization algorithm. J Intell Fuzzy Syst. 2018;35(3):2813–9. doi:10.3233/jifs-169634.
7. Ostachowicz W, Soman R, Malinowski P. Optimization of sensor placement for structural health monitoring: a review. Struct Health Monit. 2019;18(3):963–88. doi:10.1177/1475921719825601.
8. Kim SH, Cho C. Effective independence in optimal sensor placement associated with general Fisher information involving full error covariance matrix. Mech Syst Signal Process. 2024;212:111263. doi:10.1016/j.Ymssp.2024.111263.
9. Huang J, Guo K, Liu X, Zhang Z. Residual stress prediction across dimensions using improved radial basis function based eigenstrain reconstruction. Mech Mater. 2023;185:104779. doi:10.1016/j.mechmat.2023.104779.
10. Zhu Y, Meng X, Zhang X. Performance optimization of Ti-steel laser-welded joints based on optimized support vector machine and multi-objective salp Swarm Algorithm. SAE Int J Mater Manf. 2024;18(2):143–52. doi:10.4271/05-18-02-0010.

11. Braun M, Neuhäusler J, Denk M, Renken F, Kellner L, Schubnell J, et al. Statistical characterization of stress concentrations along butt joint weld seams using deep neural networks. Appl Sci. 2022;12(12):6089. doi:10.3390/app12126089.
12. Krishna SR, Sathish J, Tarun M, Jones VS, Vamsi SR, Sree SJ. A support vector machine-based intelligent system for real-time structural health monitoring of port tower cranes. Fail Anal and Preven. 2024;24(6):2543–54. doi:10.1007/s11668-024-02049-8.
13. Feng Y, Liu Y, Wang J, Li R. Research on residual stresses distribution of stiffened plate structure after induction heating based on SVM. In: Proceedings of the 32nd International Ocean and Polar Engineering Conference; 2022 Jun 5–10; Shanghai, China. p. ISOPE–I–22-385.
14. Gadallah R, Shibahara M. Stress concentration in T-butt joints: effects of weld strength and loading patterns. Constr Steel Res. 2025;226:109289. doi:10.1016/j.jcsr.2024.109289.
15. Melucci ML, Shojai S, Tanvir MH, Braun M. Statistical correlation of 3D scanned weld geometry distributions and fatigue life for different welding methods. Weld World. 2026;70(1):209–26. doi:10.1007/s40194-025-02191-3.
16. Huang N. Research on fatigue life prediction method for large structural components [dissertation]. Changsha, China: Central South University; 2013. (In Chinese). doi:10.7666/d.Y2424903.
17. Radaj D, Sonsino CM, Fricke W. Fatigue assessment of welded joints by local approaches. 2nd ed. Cambridge, UK: Woodhead Publishing; 2006.
18. Chen J. Research on fatigue failure mode and maintenance reinforcement of main girder structure of metallurgical Crane [dissertation]. Nanjing, China: Southeast University; 2021. (In Chinese). doi:10.27014/d.cnki.gdnau.2021.002122.
19. Ji J, Zhang C, Kodikara J, Yang SQ. Prediction of stress concentration factor of corrosion pits on buried pipes by least squares support vector machine. Eng Fail Anal. 2015;55:131–8. doi:10.1016/j.engfailanal.2015.05.010.
20. Yutai Y, Weizhe S, Guoshao S. A Novel support-vector-machine-based grasshopper optimization algorithm for structural reliability analysis. Buildings. 2022;12(6):855. doi:10.3390/buildings12060855.
21. Hectors K, De Waele W. Cumulative damage and life prediction models for high-cycle fatigue of metals: a review. Metals. 2021;11(2):204. doi:10.3390/met11020204.